Simulation and experimental characterization of VC precipitation and recovery stress formation in an FeMnSi-based shape memory alloy

Yajiao Yang [a,b], Christian Leinenbach [a,c,*], Moslem Shahverdi [a,d]

[a] *Empa, Swiss Federal Laboratories for Materials Science and Technology, Dübendorf, Switzerland*
[b] *Laboratory for Multifunctional Ferroic Materials, ETH, Zürich, Switzerland*
[c] *Laboratory for Photonic Materials and Characterization, École Polytechnique Fédérale de Lausanne, 1015 Lausanne, Switzerland*
[d] *School of Civil Engineering, University of Tehran, 16th Azar Street, Tehran, Iran*

ABSTRACT

In this study, TC-PRISMA was employed to simulate the precipitation (number density and radius) of an FeMnSi-based shape memory alloy (FeMnSi-SMA), with a chemical composition of Fe–17Mn–5Si–10Cr–4Ni-1(V, C) (wt%), during one-step and two-step aging processes. In addition, transmission electron microscopy (TEM) was used to study the microstructures of the specimens, particularly the VC precipitates, under several selected two-step aging conditions to validate the simulation results. Furthermore, thermomechanical characterization was conducted to investigate the recovery stress of the FeMnSi-SMA under the selected two-step aging conditions. It was found that, compared to only one-step aging, the first aging at a lower temperature (600 °C) followed by a second aging at a higher temperature (670 °C) can take advantage of both high nucleation rate and high growth rate. This achieves a similar precipitation state in a significantly shorter time (approximately 1/6 of the total duration of the one with one-step aging). The recovery stress value (509 MPa) corresponding to the two-step aging condition (first step: 600 °C for 20 h; second step: 670 °C for 6 h) shows a similar stress value range (514 MPa) corresponding to the one-step aging condition (600 °C for 144 h); however, the fracture strain is 40% higher. The number density and VC radii simulated by TC-PRISMA are generally consistent with the TEM observations.
© 2023 The Authors. Published by Elsevier B.V. This is an open access article under the CC BY license (http://creativecommons.org/licenses/by/4.0/).

1. Introduction

FeMnSi-based shape memory alloys (FeMnSi-SMAs) have been widely used in civil engineering (e.g., concrete reinforcement) [1–8] because of their low cost, good thermomechanical properties, and shape memory effect (SME) [9–14]. The governing mechanism of the SME of FeMnSi-SMAs is the reversible phase transformation between face-centered cubic (FCC) γ-austenite and hexagonal close-packed (HCP) ε-martensite [15]. During the deformation of the FeMnSi-SMA, the γ-austenite can transform into ε-martensite. Moreover, mechanically induced ε-martensite can transform back into γ-austenite upon activation (i.e., heating); therefore, it can recover the shape of an FeMnSi-SMA to some extent.

The recovery stress, which is determined by maintaining the strain constant during activation, is an important thermomechanical property of FeMnSi-SMAs. The recovery stress can be employed to assess the reinforcement potential of FeMnSi-SMAs in real structures

(e.g., concrete) [16]. Efforts have been made to enhance the recovery stress of FeMnSi-SMAs, such as employing various thermomechanical treatments [17,18], adjusting the carbon composition [19], and changing the aging conditions [20,21]. In a recent study [21], a comprehensive testing program was designed and conducted to investigate the recovery stress and microstructure of an FeMnSi-SMA as a function of aging conditions (e.g., aging time and temperature). It was found that the specimen exhibited the maximum recovery stress when aged at 600 °C for 144 h. Under such aging conditions, the precipitates were randomly distributed, both on stacking faults and in the austenite matrix, and had high number density and adequate size. Such precipitate formation in the alloy resulted in an optimal combination of a high yield stress and a pronounced γ→ε transformation during the pre-straining process, leading to maximum recovery stress. However, 144 h of aging is too long and cost-inefficient for industrial manufacturing, and this indicates a need to accelerate the aging process, e.g. by a so-called "two-step aging". Such a two-step aging strategy has been widely used for different alloys to optimize the precipitate formation process and improve their mechanical properties [22–26]. Pashley et al. [25] investigated the effect of two-step aging on precipitate

---

formation in an Al-Mg-Si alloy. Their results showed that the clusters formed during the first low-temperature aging might provide numerous precipitation nuclei; therefore, fine homogeneous precipitation could occur during the second step of aging at higher temperatures. Epicier et al. [26] conducted a two-step aging (10 h at 700 °C followed by 10 days at 800 °C) to accelerate the aging process in a model Fe–C–V steel and obtained vanadium carbide precipitates with the desired size and number density for a reasonable aging duration. Conversely, for one-step aging at 700 °C, a duration as long as 100 days would have been required to form the comparable precipitates [26]. Van Aswegen et al. [23] found that the precipitation resulting from 24 h of aging at 700 °C in Cr-Ni austenitic steels was very fine and grew slowly. The subsequent second step of aging at 850 °C could significantly increase the growth rate of precipitate, and the achieved precipitate size after aging for 1 h at 850 °C could be comparable to the size obtained after 1000 h of aging at 700 °C.

Quantitative modelling and simulation of precipitate reactions using TC-PRISMA, which can provide insights pertaining to the precipitation kinetics during heat treatment, has been widely used to investigate the precipitation processes for different alloys [27–29]. Sheng et al. [27] employed TC-PRISMA to study Cu precipitation in precipitation-hardening stainless steels and found that the simulations accurately represented the experimental observations during aging. Sanhueza et al. [28] experimentally and theoretically investigated the precipitation kinetics of second phases (e.g., $M_{23}C_6$) in 10.5% Cr heat-resistant steel. Their TC-PRISMA predictions regarding $M_{23}C_6$ carbides were in good agreement with the experimental findings. In addition, Jha et al. [29] used TC-PRISMA to study the Fe_3Si phase precipitation kinetics in Fe-Si-Nb-B-Cu alloys during heat treatment. Their predictions supported that TC-PRISMA could consistently predict the nucleation rate and number density of the Fe_3Si phase.

In this study, the effect of two-step aging conditions (e.g., aging temperature and time) on precipitate formation, as well as on the recovery stress in FeMnSi-SMA, with an activation temperature up to 160 °C, were investigated. TC-PRISMA was employed to simulate the size and number density of precipitates and to comprehensively understand precipitate formation during one- and two-step aging conditions.

2. Material

The material investigated in the current study, similar to that studied in [21], was a hot-rolled strip with a chemical composition of Fe–17Mn–5Si–10Cr–4Ni-1(V, C) (wt%). The specimens were solutionized at 1070 °C for two hours to eliminate the residual precipitates from the original production. This was followed by water quenching to avoid the formation of precipitates during cooling. The solutionized specimens were subsequently machined into dog-bone geometry for two-step aging and thermomechanical experiments.

3. Simulation

Modelling and simulation of the precipitation (during the aging of the FeMnSi-SMA) were carried out using the TC-PRISMA (version 2021b) precipitation module. This module is based on the Langer–Schwartz theory [29,30] and employs the Kampmann–Wagner numerical (KWN) approach [29–31] to simulate precipitate nucleation, growth, and coarsening in multicomponent and multiphase alloy systems. The nucleation model in TC-PRISMA was developed based on the classical nucleation theory and has been extended for nucleation in multicomponent systems. TC-PRISMA can simulate both heterogeneous and homogeneous nucleation, where heterogeneous nucleation sites can include dislocations, grain edges, and boundaries [30]. Furthermore, TC-PRISMA includes both advanced and simplified growth models. The advanced model takes

into consideration both high supersaturation and cross-diffusion and identifies the change in the operating tie-line from the solution of flux-balance equations. This allows the spontaneous transition of the growth mode [30,32,33]. The simplified growth model uses a tie line across the bulk composition throughout the simulation, and this significantly reduces calculation time [30,32,33]. In this model, homogeneous nucleation of precipitates in the austenite matrix was assumed (i.e., bulk nucleation in TC-PRISMA), and a simplified growth model was used, in which the time-dependent nucleation rate, $J(t)$, is given by [34,35]:

$$J(t) = J_s \exp\left(-\frac{\tau}{t}\right), \tag{1}$$

where J_s is the nucleation rate in the steady state, τ is the incubation time required to achieve steady-state nucleation conditions, and t is the isothermal reaction time [36]. J_s is calculated by

$$J_s = Z\beta^*N_0 \exp\left(\frac{-\Delta G^*}{kT}\right), \tag{2}$$

where Z is the Zeldovich factor, β^* is the rate of formation of the critical nucleus, N_0 is the number of available nucleation sites per unit volume, ΔG^* is the Gibbs energy of formation of a critical nucleus, T is the absolute temperature, and k is Boltzmann's constant [36].

The Gibbs energy of formation of a critical nucleus is given as follows

$$\Delta G^* = \frac{16\pi\sigma^3}{3(\Delta G_m^{\alpha\to\beta}/V_m^\beta)}, \tag{3}$$

where σ is the interfacial energy, $\Delta G_m^{\alpha\to\beta}$ is the molar Gibbs energy change for the β precipitate formation, and V_m^β is the molar volume of the β precipitate phase. Further details regarding the calculation of Z and β^* can be found in [36].

In the simplified growth rate model, the interface velocity v can be derived as follows:

$$v = \frac{K}{r}\left[\Delta G_m - \frac{2\sigma V_m^\beta}{r}\right] = \frac{2\sigma V_m^\beta K}{r}\left[\frac{1}{r^*} - \frac{1}{r}\right], \tag{4}$$

where ΔG_m is the nucleation driving force, r^* is the radius of the critical nuclei, and K is the kinetic parameter, which can be derived as:

$$K = K_{sphere}^{simplified} = \left[\sum_i \frac{(X_i^{\beta/\alpha}(r) - X_i^{\alpha/\beta}(r))^2 \xi_i}{X_i^{\alpha/\beta} M_i}\right]^{-1} \tag{5}$$

where $X_i^{\beta/\alpha}(r)$ and $X_i^{\alpha/\beta}(r)$ are the interface compositions for the precipitate and matrix phases, respectively, M_i is the corresponding atomic mobility in the matrix, and ξ_i is the effective diffusion distance factor [36].

FCC austenite and FCC_A1#2 VC [37–39] in the TC-PRISMA database were selected as the matrix and precipitation phases, respectively. Based on the lattice parameters $a_\gamma = 3.6069$ Å and $a_{VC} = 4.0978$ Å [38], the molar volumes of matrix and VC precipitate were calculated to be 7.06 cm³/mol and 10.36 cm³/mol, respectively. Several user-defined parameters were adopted from previous studies [21,40], as listed in Table 1. Other parameters in the simulation were set as the default values in TC-PRISMA. The output of the simulation was the evolution of the mean radius and number density as a function of time.

Table 1
Adopted user-defined parameters in the simulations.

Grain size [μm]	Dislocation density [m⁻²]	VC molar volume [cm³mol⁻¹]	Matrix molar volume [cm³mol⁻¹]
63[21]	10¹¹[40]	10.36	7.06

Table 2

Summary of the conducted simulations and experiments. 'Thermomechanical experiment' is denoted as 'TM experiment' in the fourth column.

Aging condition	Simulation	TEM	TM experiment
600 °C (144 h)	✓	✓[21]	✓[21]
632 °C (72 h)	✓		✓[21]
660 °C (9 h)	✓	✓[21]	✓[21]
600 °C (20 h) + 670 °C (2 h)	✓	✓	✓
600 °C (20 h) + 670 °C (4 h)	✓		✓
600 °C (20 h) + 670 °C (6 h)	✓	✓	✓
600 °C (20 h) + 670 °C (8 h)	✓		✓
600 °C (20 h) + 670 °C (10 h)	✓		✓
600 °C (4 h) + 670 °C (6 h)	✓	✓	✓
600 °C (10 h) + 670 °C (6 h)	✓		✓
600 °C (20 h) + 670 °C (6 h)	✓		✓
600 °C (41 h) + 670 °C (6 h)	✓	✓	✓

The simulation results are summarized in Table 2. The aims of conducting the one-step aging simulation were to determine the interfacial energy and examine the effectiveness of the developed simulation by comparing the simulated results with experimental observations in [21]. In the two-step aging simulation, 600 °C and 670 °C were selected as the temperatures for the first and second aging steps, respectively. Simulations with different aging times in the two-step aging were designed to determine the optimal two-step aging conditions, which could lead to similar precipitate formation (i.e., number density and mean radius) as that in the one-step aging process (i.e., 144 h at 600 °C) whereby maximum recovery stress was achieved.

4. Experimental details

4.1. One-step and two-step aging

In one-step aging, a sample is subjected to a certain duration of heat treatment at a constant temperature. A detailed introduction to one-step aging can be found in Ref.[21]. In this study, two-step aging was conducted aiming to accelerate the aging process while generating similar precipitates, as that achieved by one-step aging in a previous study [21]. The first step of aging occurs at a low temperature (e.g., 600 °C) for having a high precipitate nucleation rate and, accordingly, high precipitate number density. The second aging step occurs at a relatively high temperature to accelerate the precipitate growth to the desired conditions and reduce the overall aging duration. The experimental observations of one- and two-step aging were then used to validate the outcomes of the precipitation simulation.
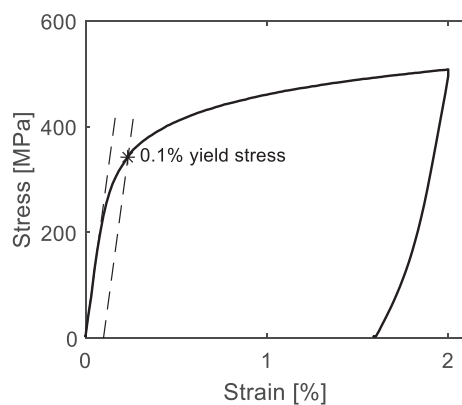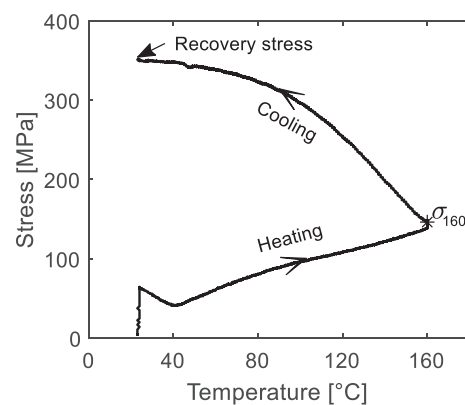
4.2. Thermomechanical experiments

The recovery stress of the specimens subjected to two-step aging was determined by pre-straining and activation experiments, and the details pertaining to the thermomechanical experiments are listed in Table 2. Pre-straining is a process during which the specimen is loaded onto a target strain (2% in this study), followed by full unloading. Activation is the process of heating a prestrained FeMnSi-SMA and cooling it to room temperature while maintaining the specimen at a constant strain. The maximum activation temperature used in this study was 160 °C and the heating and cooling rates were 2 °C /min. The recovery stress, σ_{rec}, was measured after the activation process and at room temperature (23 °C). Typical prestraining (stress-strain) and activation (stress-temperature) curves are shown in Fig. 1. (a) and (b). Both pre-straining and activation experiments were conducted using a Z020 Zwick tensile test machine. Strain during activation was measured and controlled using a mini-MFA 2 type extensometer. A more detailed experimental description can be found in Ref.[21].

4.3. Transmission electron microscopy

Based on the outcomes of the two-step aging simulation, several two-step aging conditions were selected for the microstructure examination and are listed in Table 2. The number density and mean radius of the precipitates under selected conditions were measured using transmission electron microscopy (TEM, JEM-2200FS JEOL). TEM is a powerful technique for characterizing the microstructure (e.g., precipitates and dislocations) of an alloy by analyzing the electron signals generated by the interaction of a high-energy beam of electrons with the alloy. All TEM specimens were mechanically ground and polished to a thickness of $\sim$160 µm and then punched into 3 mm round disks. Finally, the discs were electropolished (Standard A2 Struers solution) at approximately 24 V and $-$6 °C.

5. Results

5.1. One-step aging

The simulation results were highly dependent on the interfacial energy values in the TC-PRISMA. A one-step aging simulation was conducted to determine the value of the interfacial energy that led to the best match between the simulated and experimental results. Table 3 compares the experimentally determined values for the precipitate number densities and radii with the simulation outcomes by using different interfacial energies varying from 0.68 to

(a)

(b)

Fig. 1. (a) Typical pre-straining curve for an FeMnSi-SMA specimen. (b) Typical activation curve: the specimen was heated from room temperature to 160 °C and subsequently cooled to room temperature.

Table 3

Comparison of the simulated and experimental results for one-step aging. The simulated radius and number density values vary with input interfacial energy values ranging from 0.68 to 0.71 J/m^2.

Conditions		TEM	0.68	0.69	0.7	0.71
600 °C for 144 h	Radius [nm]	3.3	3.2	3.7	4.3	4.9
	Number density [1/m^3]	1.5E22	8.1E22	5.3E22	3.5E22	2.2E22
660 °C for 9 h	Radius [nm]	4.5	5.1	5.8	6.5	7.2
	Number density [1/m^3]	6.7E21	1.9E22	1.2E22	7.3E21	4.4E21

0.71 J/m^2. It can be seen that, as the interfacial energy increases, the simulated precipitate radii increase at both 600 and 660 °C, while the number density decreases. A detailed comparison shows that an interfacial energy value of 0.70 J/m^2 leads to the best match and was therefore used in TC-PRISMA for the two-step aging.

Fig. 2. shows the simulated time evolution of number density and mean radius of precipitates for the one-step aging at 600, 632, and 660 °C. It can be seen that the number density increases quickly in the early stage of aging and then becomes stable over a longer time. The radius of precipitates increases over aging time and gradually becomes stable for the temperatures 600 °C and 632 °C. For a given aging time, the number density increases with decreasing aging temperature, while the mean radius increases with increasing aging temperature. Such a trend is consistent with the experimental observations in a previous study [21]. Furthermore, the simulated number density and mean radius of the precipitates are comparable with the experimental results in [21], given in Table 3. The good

consistency between simulations and experiments validates the developed precipitation model.

5.2. Two-step aging

5.2.1. Effect of the aging duration of the second step aging on the precipitates

Fig. 3. and Fig. 4. show the simulated time evolution of mean radius and number density of precipitates, respectively, for the two-step aging conditions with different second step aging durations (first step: 600 °C for 20 h; second step: 670 °C for 2–10 h). For comparison, the simulated one-step aging result (600 °C for 144 h) is also included and is represented by the dotted lines. It can be observed from Fig. 3(a) that the precipitate growth rate (i.e., the slope of the mean radius vs. time) increases significantly upon the onset of the second step of aging, which is attributed to the much higher diffusion rates at a higher aging temperature [41]. The zoomed-in
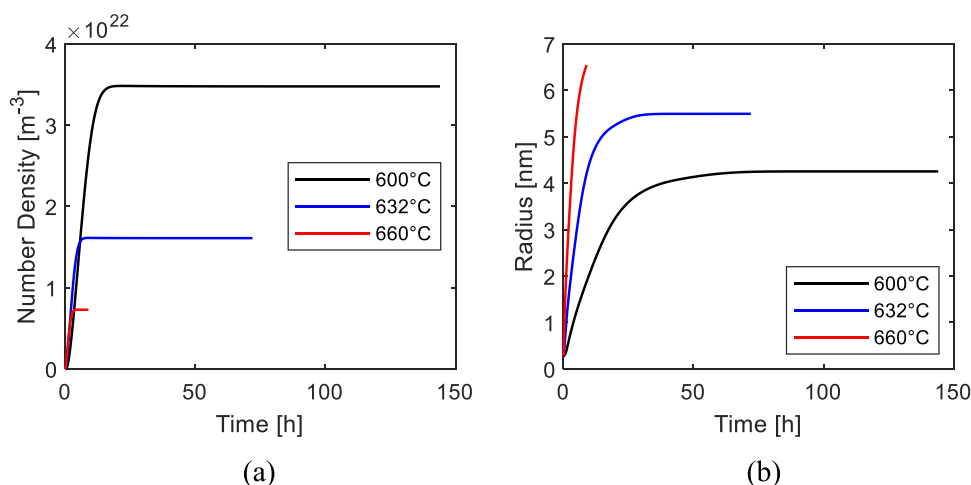

(a)   (b)

Fig. 2. Simulated number density (a) and mean radius (b) of precipitates as functions of time for the one-step aging at 600, 632, and 660 °C.

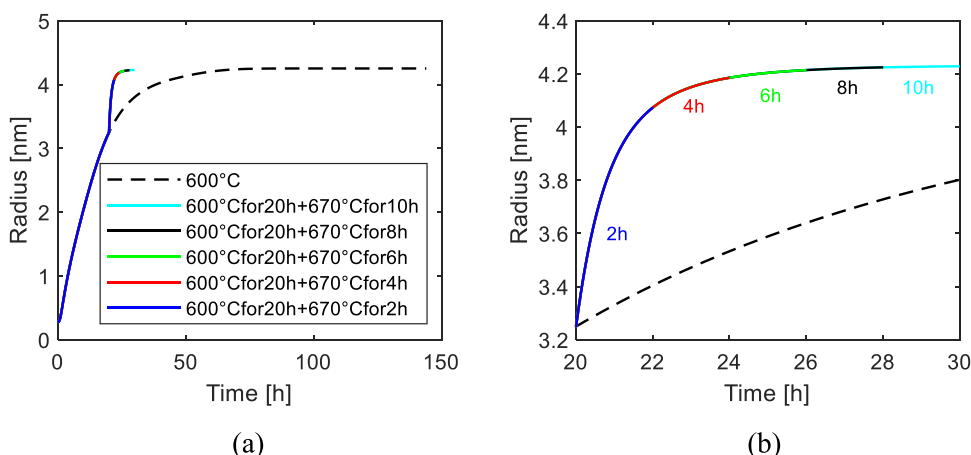

(a)   (b)

Fig. 3. Simulated time evolution of mean radius of precipitates for the two-step aging with different second step duration (a); Zoomed-in plot of second step of aging (b) in (a).
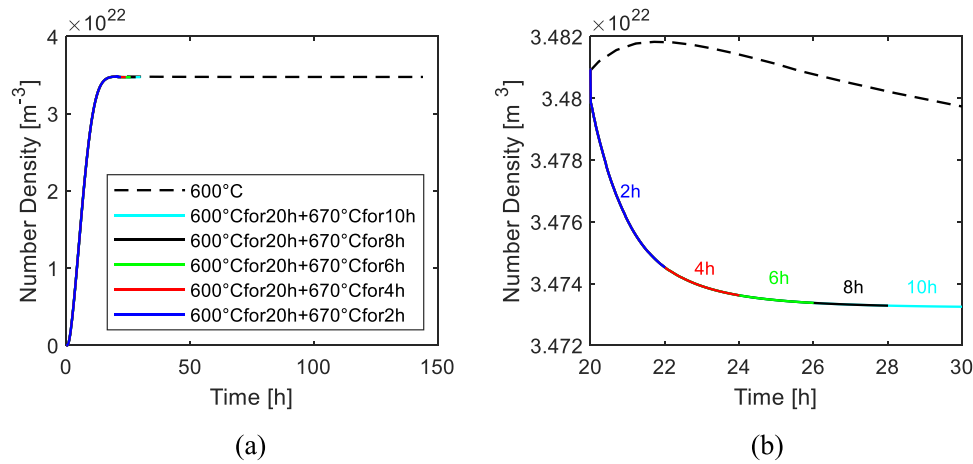
Fig. 4. Simulated time evolution of number density of precipitates for the two-step aging with different second step duration (a); Zoomed-in plot of second step of aging (b) in (a).

plot of the second step in Fig. 3(b) indicates that the mean radius of the precipitates increased quickly during the first 2 h and then became stagnant after 6 h. After aging for 6 h during the second step, the mean radius of the precipitates was comparable to that achieved in the desired one-step aging (144 h at 600 °C). Fig. 4(a) shows that the number density of precipitates after the first step (i.e., 20 h at 600 °C) was close to that obtained in the one-step aging. However, as shown in Fig. 4(b), the number density started to decrease slightly upon the onset of the second step. According to the simulation results, the generated precipitates after the two-step aging (first step: 600 °C for 20 h; second step: 670 °C for 6 h) are similar to those achieved in the desired one-step aging (144 h at 600 °C), in terms of mean radius and number density.

5.2.2. Effect of the aging duration of the first step on the precipitates

Fig. 5(a) and (b) show the simulated time evolution of number density and mean radius, respectively, of precipitates for the two-step conditions with different first step durations (first step: 600 °C for 4–41 h; second step: 670 °C for 6 h). The simulated one-step aging result was also included for comparison with the results of the two-step aging. It can be seen from Fig. 5(a) that, for the first step of aging at 600 °C, the number density of precipitates after 4 h and 10 h was much lower than that after 20 h and 41 h, while the number density after 41 h was only slightly higher than that after 20 h.

Fig. 5(b) shows that the mean radius of the precipitates increases with a shorter first-step duration. During the second step, the mean radius increased more quickly for the specimen experiencing the

shorter first step. At the end of the second step, the mean radius of the precipitates was the largest for the specimen with the shortest first step (i.e., 4 h), and there was no considerable difference between the specimens with 20 h and 41 h of aging during the first step. Therefore, there are two two-step aging conditions: first step: 600 °C for 20 h or 41 h; second step: 670 °C for 6 h, which can lead to similar precipitate formation as the one-step aging for 144 h at 600 °C.

5.3. TEM observations of precipitates

Based on the simulation results, several two-step aging conditions were selected for the characterization of the precipitates by TEM. The obtained bright field (BF) images are shown in Fig. 6. It can be seen that, for all the selected conditions, fine precipitates were evenly dispersed in the austenite matrix and on/near stacking faults. In the high-magnification images, fine coherent precipitates with coffee-bean contrast can be observed, which are induced by the displacement field of a coherent precipitate [42]. The number density and mean radius of the precipitates for each condition were measured using the ImageJ software. The thickness of the TEM foil was estimated to be 150 nm using convergent beam electron diffraction under two-beam conditions.

The experimental results obtained using TEM are compared with the simulated outcomes in Table 4 (first step: 600 °C for 20 h; second step: 670 °C for 2 and 6 h), Table 5 (first step: 600 °C for 4, 20, and
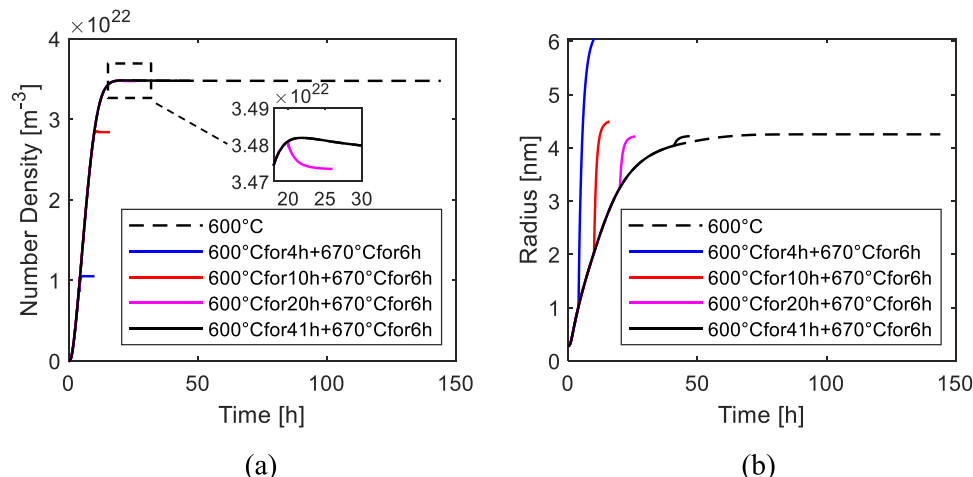

Fig. 5. Simulated time evolution of number density (a) and mean radius (b) of precipitates for the two-step aging with different first step duration.

600 °C (20 h) + 670 °C (2 h)   600 °C (20 h) + 670 °C (6 h)   600 °C (41 h) + 670 °C (6 h)   600 °C (4 h) + 670 °C (6 h)

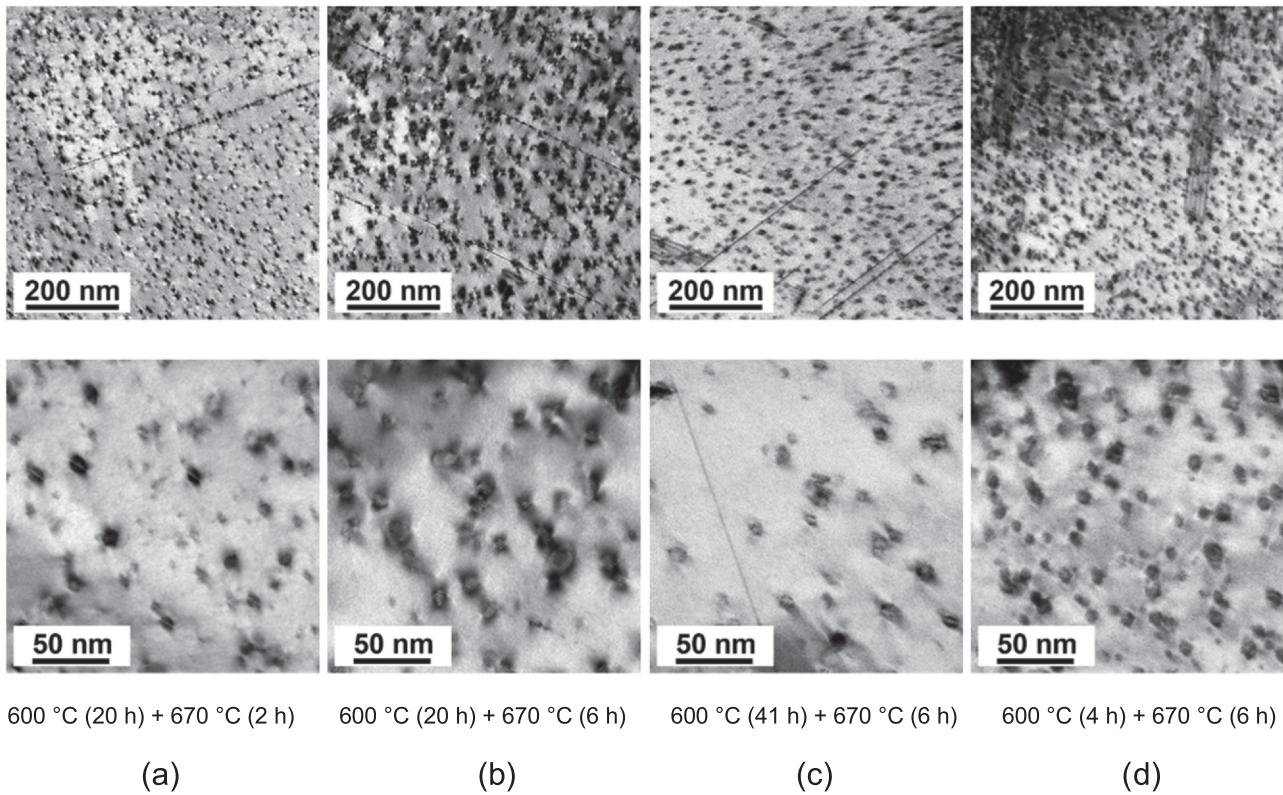(a)   (b)   (c)   (d)

Fig. 6. BF transmission electron microscopy (TEM) images of the FeMnSi-SMA for the different two-step aging conditions.

41 h; second step: 670 °C for 6 h), and Table 6 (one-step and several selective two-step aging conditions).

5.4. Recovery stress of FeMnSi-SMAs after two-step aging

Fig. 7(a) shows the evolution of the stress-temperature during the activation of the specimens after the two-step aging process (first step: 600 °C for 20 h; second step: 670 °C for 2–10 h). It can be seen that the stress at the activation temperature 160 °C, σ_{160}, increases with increasing aging duration in the second step. When the second step duration reached 6 h, there was no significant increase in the value of σ_{160} and recovery stress. Two specimens with the same two–steps aging condition (first step: 600 °C for 20 h; second step: 670 °C for 6 h) were examined for the recovery stress. The good consistency of the activation curves indicates good repeatability of the experiments.

Fig. 7(b) shows the evolution of stress-temperature during the activation of the specimens experiencing two-step aging (first step: 600 °C for 4–41 h; second step: 670 °C for 6 h). It can be seen that the values of σ_{160} for the 4–20 h duration time remain almost the same. However, as the duration increases, the recovery stress continued to increase under these conditions because the stress-temperature curves become steeper. Finally, after 41 h, σ_{160} starts to increase, but there is no noticeable increase in the final recovery stress value.

In Table 7, it can be observed that the fracture strain of the specimen for the two-step aging condition (first step: 600 °C for 20 h; second step: 670 °C for 6 h) is 40% higher than that for the one-

step aging condition (144 h at 600 °C). However, the recovery stresses of the two-and one-step conditions are only slightly different.

6. Discussion

TC-PRISMA simulations were conducted to provide a better understanding of the precipitation kinetics during two-step aging and to facilitate optimization of the aging conditions for FeMnSi-SMAs. The simulated results show that two two-step aging conditions (i.e., first step: 600 °C for 20 h or 41 h; second step: 670 °C for 6 h) can form the comparable size and number density of precipitates with the precipitates aged for 144 h at 600 °C. A comparison of the experimental and simulated results in Tables 4 and 5 demonstrates that the simulated outcomes are generally consistent with the experimental observations, especially the evolution trend of the number density and mean radius values of precipitates under different conditions. As shown in Table 4, in the second aging step, the number density decreases, and the mean radius increases over the aging time. Furthermore, the magnitudes of the mean radii of the precipitates are comparable between the simulation and the experiment. However, the number density of the precipitates in the experiment was lower than that in the simulation. This may be due to the following reasons. From an experimental point of view, some very fine precipitates may be too small to be observed by TEM. Some fine precipitates could be located under the coarse precipitates and therefore could not be counted, that is, underestimation of the

Table 4
Comparison of the simulated and experimental results for the aging conditions (first step: 600 °C for 20 h; second step: 670 °C for 2 and 6 h).

Condition	TEM		Simulation	
	Radius [nm]	NrDensity [1/m^3]	Radius [nm]	NrDensity [1/m^3]
600 °C (20 h) + 670 °C (2 h)	2.9	1.4E+22	4.1	3.5E+22
600 °C (20 h) + 670 °C (6 h)	3.8	1.1E+22	4.2	3.5E+22

Table 5
Comparison of the simulated and experimental results for the aging conditions (first step: 600 °C for 4, 20, and 41 h; second step: 670 °C for 6 h).

Condition	TEM		Simulation	
	Radius [nm]	NrDensity [1/m³]	Radius [nm]	NrDensity [1/m³]
600 °C (4 h) + 670 °C (6 h)	5.2	7.0E+21	6.0	1.1E+22
600 °C (20 h) + 670 °C (6 h)	3.8	1.1E+22	4.2	3.5E+22
600 °C (41 h) + 670 °C (6 h)	3.9	1.6E+22	4.2	3.5E+22

Table 6
Comparison of the results between one-step and two-step aging.

Condition	TEM		Simulation	
	Radius [nm]	NrDensity [1/m³]	Radius [nm]	NrDensity [1/m³]
600 °C for 144 h	3.3	1.5E+22	4.3	3.5E+22
600 °C (20 h) + 670 °C (6 h)	3.8	1.1E+22	4.2	3.5E+22
600 °C (41 h) + 670 °C (6 h)	3.9	1.6E+22	4.2	3.5E+22

precipitate density. From a simulation perspective, TC-PRISMA is based on several approximations (e.g., thermodynamic and diffusion mobility databases) and assumptions (e.g., homogeneous nucleation and simplified growth models), which could lead to some uncertainties. For example, the selection of a lower interfacial energy may result in the prediction of a higher precipitate nucleation rate and, accordingly, a higher precipitate number density. A change in the assumptions and input data for the simulation could alter the simulated results. Despite such uncertainties, the good consistency of the evolution trend of the number density and mean radius values of the precipitates still demonstrates the capability of the developed TC-PRISMA simulation.

Table 5 shows that, for the longer aging time in the first step, the number density after the second step (6 h at 670 °C) is larger, while the mean radius of the precipitate for the 20 h and 41 h first step is smaller than that for the 4 h. The good consistency between the experiment and simulation demonstrates the effectiveness of the precipitation simulation and also confirms that two two-step aging conditions (first step: 600 °C for 20 and 41 h; second step: 670 °C for 6 h) can result in similar precipitate formation as the one-step aging (144 h at 600 °C), as shown in Table 6.

The effect of two-step aging on the recovery stress can be understood by analyzing the activation curve of the FeMnSi-SMAs. Fig. 7(a) shows that the stress at the activation temperature of 160 °C, σ_{160}, is larger for the specimen with a longer aging duration in the second step. σ_{160} is determined by the martensite-to-austenite

transformation. A larger σ_{160} is attributed to more martensite-to-austenite transformation during the heating process, which implies a larger amount of austenite-to-martensite transformation during pre-straining [21]. A longer aging duration in the second step can lead to larger mean radii of the precipitates and a larger σ_{160}. This is in good agreement with the experimental observations in [21,38], where it was found that large precipitates could facilitate austenite-to-martensite transformation during deformation/prestraining. The final recovery stress was also determined by the ease with which the material was produced during the cooling process. A lower yield stress can lead to early yielding (i.e., the stress-temperature curve during the cooling process is easily bent), thus resulting in a smaller recovery stress. Fig. 7(b) shows that the recovery stress increases with the aging duration (4–20 h) in the first step, although σ_{160} for all conditions is close. This is because the number density of the precipitates increased with the aging duration in the first step. A higher number density of precipitates can lead to a larger yield stress of the alloy; therefore, the alloy is not easily formed during the cooling process, and this leads to a higher recovery stress. As the first step time was further increased to 41 h, there was no further increase in the recovery stress value. Experiments and simulations consistently show that these two two-step conditions (first step: 600 °C for 6 h; second step: 20 and 41 h) can lead to a similar precipitate formation as the one-step aging for 144 h at 600 °C. The obtained recovery stress under these two two-step conditions is approximately 509 MPa, which is comparable to the maximum recovery stress of 514 MPa achieved by the one-step aging at 144 h at 600 °C. This finding further demonstrates the effectiveness of the developed simulation. Such time efficiency, especially for the condition of 600 °C for 20 h followed by 670 °C for 6 h (in total 26 h), significantly reduces process time in an industrial production process, achieves comparable recovery stress to the 600 °C for 144 h aging, and lowers the manufacturing expenditure.

Table 7 shows that the fracture strain of the specimen for the two-step aging condition (first step: 600 °C for 20 h; second step: 670 °C for 6 h) is much higher than that for the one-step aging condition (144 h at 600 °C), while their recovery stress is only
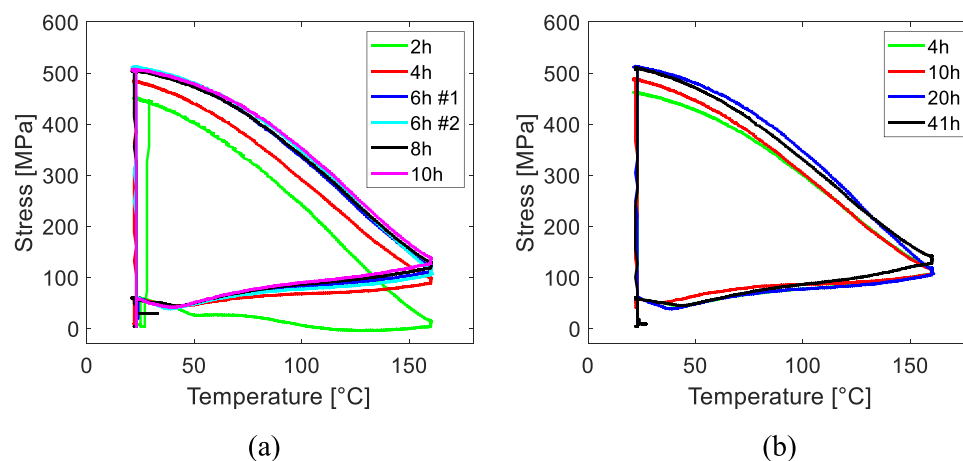

Fig. 7. Activation curve of the specimens with different two-step aging conditions: first step: 600 °C for 20 h; second step: 670 °C for 2–10 h (a), and first step: 600 °C for 4–41 h; second step: 670 °C for 6 h (b).

Table 7
Comparison of the fracture strain between one-step and two-step aging.

Aging conditions	Failure strain [%]	Average strain [%]	Recovery stress [MPa]
600 °C (20 h) + 670 °C (6 h) (Specimen 1)	13.5	13.4	509
600 °C (20 h) + 670 °C (6 h) (Specimen 2)	13.3		
600 °C (144 h) (Specimen 1)	9.7	9.5	514
600 °C (144 h) (Specimen 2)	8.8		
600 °C (144 h) (Specimen 3)	10.0		
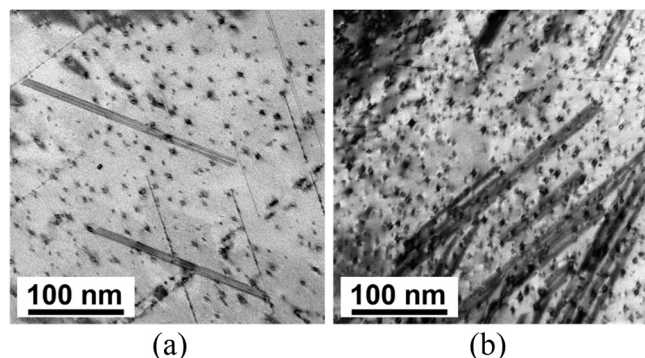
Fig. 8. TEM images of the specimen for the two-step aging condition (first step: 600 °C for 20 h; second step: 670 °C for 6 h) (a) and the one-step aging condition (144 h at 600 °C) (b).

slightly lower. One possible reason could be that the precipitate number and stacking fault densities for the two-step aging condition are lower than that for the one-step aging (Fig. 8). Such lower precipitate number would lead to lower yield stress (i.e. less precipitate hardening effect), and lower stacking fault densities might provide less obstacles for dislocation movement, and consequently result in higher fracture strain. This ductility increase for the two-step aging is very beneficial for civil engineering related applications of the FeMnSi-SMAs. However, a more detailed study on this phenomenon would need to be undertaken in the future.

7. Concluding remarks

The two-step aging treatment combines both a high nucleation rate and growth rate of precipitates, thus improving the industry's cost efficiency and carbon emissions. By using the TC-PRISMA module to simulate one- and two-step aging processes and conducting TEM observations and thermomechanical experiments on the novel FeMnSi-SMA, the following conclusions can be drawn:

i. The onset of the second step of aging at a high temperature (670 °C) can immediately facilitate precipitation growth. Initially, the radius of VC increased rapidly. After 6 h, the growth rate stagnated, and further increasing the duration had no distinct effect on the VC radius. Meanwhile, with the addition of the second step of aging, the VC number density remained almost the same compared to the 600 °C for 144 h aging. A larger VC with a similar number density can promote martensite formation and the shape memory effect in the alloy, thereby leading to a higher σ_{160}. This results in higher recovery stresses.

ii. Longer (e.g., 20 h and 40 h) aging durations at a lower temperature (600 °C) can significantly expand the VC number density. Because a larger number density is beneficial for precipitation hardening, the recovery stress is improved because the stress-temperature curve becomes steeper during the cooling process owing to precipitation hardening.

iii. By applying two-step aging procedure, the FeMnSi-SMA achieved a recovery stress value of 509 MPa (first step: 600 °C for 20 h; second step: 670 °C for 6 h), showing similar recovery stress

(514 MPa) to that of one-step aging (600 °C for 144 h). However, the fracture strain was 40% higher.

iv. TC-PRISMA can simulate the precipitation of FeMnSi-SMAs after both one-step and two-step aging within a reasonable range. The simulated number densities and VC radii were mostly consistent with the TEM observations by employing an interfacial energy 0.70 J/m^2. The results can be used in the heat treatment design of FeMnSi-SMAs in the future.

CRediT authorship contribution statement

Yajiao Yang: Conceptualization, Methodology, Formal analysis, Investigation, Data curation, Visualization, Writing – original draft, Writing – review & editing. **Christian Leinenbach:** Conceptualization, Methodology, Supervision, Writing – review & editing. **Moslem Shahverdi:** Conceptualization, Methodology, Funding acquisition, Supervision, Writing – review & editing.

Data Availability

The authors do not have permission to share data.

Declaration of Competing Interest

The authors declare that they have no known competing financial interests or personal relationships that could have appeared to influence the work reported in this paper.

Acknowledgements

References

[1] S. Raza, J. Michels, B. Schranz, M. Shahverdi, Anchorage behavior of Fe-SMA rebars Post-Installed into concrete, Eng. Struct. 272 (2022) 114960.

[2] S. Raza, J. Michels, M. Shahverdi, Uniaxial behavior of pre-stressed iron-based shape memory alloy rebars under cyclic loading reversals, Constr. Build. Mater. 326 (2022) 126900.

[3] B. Schranz, M.F. Nunes, C. Czaderski, M. Shahverdi, Fibre optic strain measurements for bond modelling of prestressed near-surface-mounted iron-based shape memory alloy bars, Constr. Build. Mater. 288 (2021) 123102.

[4] I. Ferretto, D. Kim, N. Della Ventura, M. Shahverdi, W. Lee, C. Leinenbach, Laser powder bed fusion of a Fe–Mn–Si shape memory alloy, Addit. Manuf. 46 (2021) 102071.

[5] A. Arabi-Hashemi, E. Polatidis, M. Smid, T. Panzner, C. Leinenbach, Grain orientation dependence of the forward and reverse fcc↔ hcp transformation in FeMnSi-based shape memory alloys studied by in situ neutron diffraction, Mater. Sci. Eng.: A 782 (2020) 139261.

[6] Yang, Y., A. Arabi-Hashemi, C. Leinenbach, and M. Shahverdi. Improvement of FeMnSi based shape memory alloys yield stress by heat treatment. in 5th SMAR Conference, Potsdam. 2019.

[7] S. Raza, B. Shafei, M.S. Saiidi, M. Motavalli, M. Shahverdi, Shape memory alloy reinforcement for strengthening and self-centering of concrete structures—State of the art, Constr. Build. Mater. 324 (2022) 126628.

[8] Y. Yang, M. Breveglieri, M. Shahverdi, Effect of phase changes on the axial modulus of an FeMnSi-shape memory alloy, Materials 14 (17) (2021) 4815.

[9] S. Kajiwara, Characteristic features of shape memory effect and related transformation behavior in Fe-based alloys, Mater. Sci. Eng.: A 273 (1999) 67–88.

[10] C. Leinenbach, H. Kramer, C. Bernhard, D. Eifler, Thermo-mechanical properties of an Fe–Mn–Si–Cr–Ni–VC shape memory alloy with low transformation temperature, Adv. Eng. Mater. 14 (1–2) (2012) 62–67.

[11] W. Lee, B. Weber, G. Feltrin, C. Czaderski, M. Motavalli, C. Leinenbach, Stress recovery behaviour of an Fe–Mn–Si–Cr–Ni–VC shape memory alloy used for prestressing, Smart Mater. Struct. 22 (12) (2013) 125037.

[12] A.V. Druker, A. Baruj, L. Isola, V. Fuster, J. Malarría, R. Bolmaro, Gaining flexibility in the design of microstructure, texture and shape memory properties of an Fe–Mn-Si-Cr-Ni alloy processed by ECAE and annealing, Mater. Des. 107 (2016) 153–162.

[13] M. Shahverdi, C. Czaderski, P. Annen, M. Motavalli, Strengthening of RC beams by iron-based shape memory alloy bars embedded in a shotcrete layer, Eng. Struct. 117 (2016) 263–273.

[14] C. Leinenbach, A. Arabi-Hashemi, W. Lee, A. Lis, M. Sadegh-Ahmadi, S. Van Petegem, T. Panzner, H. Van, Swygenhoven, *Characterization of the deformation and phase transformation behavior of VC-free and VC-containing FeMnSi-based shape memory alloys by* in situ *neutron diffraction*, Mater. Sci. Eng.: A 703 (2017) 314–323.

[15] A. Cladera, B. Weber, C. Leinenbach, C. Czaderski, M. Shahverdi, M. Motavalli, Iron-based shape memory alloys for civil engineering structures: an overview, Constr. Build. Mater. 63 (2014) 281–293.

[16] J. Michels, M. Shahverdi, C. Czaderski, Flexural strengthening of structural concrete with iron-based shape memory alloy strips, Struct. Concr. 19 (3) (2018) 876–891.

[17] A. Baruj, T. Kikuchi, S. Kajiwara, N. Shinya, Effect of pre-deformation of austenite on shape memory properties in Fe–Mn–Si-based alloys containing Nb and C, Mater. Trans. 43 (3) (2002) 585–588.

[18] C. Wang, Y. Wen, H. Peng, D. Xu, N. Li, Factors affecting recovery stress in Fe–Mn–Si–Cr–Ni–C shape memory alloys, Mater. Sci. Eng.: A 528 (3) (2011) 1125–1130.

[19] Y. Wen, N. Li, L. Xiong, Composition design principles for Fe–Mn–Si–Cr–Ni based alloys with better shape memory effect and higher recovery stress, Mater. Sci. Eng.: A 407 (1–2) (2005) 31–35.

[20] A. Arabi-Hashemi, W. Lee, C. Leinenbach, Recovery stress formation in FeMnSi based shape memory alloys: Impact of precipitates, texture and grain size, Mater. Des. 139 (2018) 258–268.

[21] Y. Yang, A. Arabi-Hashemi, C. Leinenbach, M. Shahverdi, Influence of thermal treatment conditions on recovery stress formation in an FeMnSi-SMA, Mater. Sci. Eng.: A 802 (2021) 140694.

[22] E. Elgallad, Z. Zhang, X.-G. Chen, Effect of two-step aging on the mechanical properties of AA2219 DC cast alloy, Mater. Sci. Eng.: A 625 (2015) 213–220.

[23] J. Van Aswegen, R. Honeycombe, D. Warrington, Precipitation on stacking faults in Cr-Ni austenitic steels, Acta Metall. 12 (1) (1964) 1–13.

[24] M. Czerny, G. Cios, W. Maziarz, Y. Chumlyakov, R. Chulist, Studies on the two-step aging process of Fe-based shape memory single crystals, Materials 13 (7) (2020) 1724.

[25] D. Pashley, M. Jacobs, J. Vietz, The basic processes affecting two-step ageing in an Al-Mg-Si alloy, Philos. Mag. 16 (139) (1967) 51–76.

[26] T. Epicier, D. Acevedo, M. Perez, Crystallographic structure of vanadium carbide precipitates in a model Fe–C–V steel, Philos. Mag. 88 (1) (2008) 31–45.

[27] Z. Sheng, M. Bonvalet Rolland, T. Zhou, J. Odqvist, P. Hedström, Langer–Schwartz–Kampmann–Wagner precipitation simulations: assessment of models and materials design application for Cu precipitation in PH stainless steels, J. Mater. Sci. 56 (3) (2021) 2650–2671.

[28] J. Sanhueza, D. Rojas, O. Prat, J. Garcia, R. Espinoza, C. Montalba, M. Melendrez, Precipitation kinetics in a 10.5% Cr heat resistant steel: Experimental results and simulation by TC-PRISMA/DICTRA, Mater. Chem. Phys. 200 (2017) 342–353.

[29] Jha, R., D.R. Diercks, A.P. Stebner, and C.V. Ciobanu, *Metastable phase diagram and precipitation kinetics of magnetic nanocrystals in FINEMET alloys.* arXiv preprint arXiv:1709.08306, 2017.

[30] G. Lindwall, C. Campbell, E. Lass, F. Zhang, M.R. Stoudt, A.J. Allen, L.E. Levine, Simulation of TTT curves for additively manufactured Inconel 625, Metall. Mater. Trans. A 50 (1) (2019) 457–467.

[31] M.M. Cueto-Rodriguez, E.O. Avila-Davila, V.M. Lopez-Hirata, M.L. Saucedo-Muñoz, L.M. Palacios-Pineda, L.G. Trapaga-Martinez, J.M. Alvarado-Orozco, Numerical and experimental analyses of the effect of heat treatments on the phase stability of inconel 792, Adv. Mater. Sci. Eng. 2018 (2018).

[32] Q. Chen, K. Wu, G. Sterner, P. Mason, Modeling precipitation kinetics during heat treatment with calphad-based tools, J. Mater. Eng. Perform. 23 (12) (2014) 4193–4196.

[33] Z. Hou, R.P. Babu, P. Hedström, J. Odqvist, Early stages of cementite precipitation during tempering of 1C–1Cr martensitic steel, J. Mater. Sci. 54 (12) (2019) 9222–9234.

[34] D. Kashchiev, Nucleation, Elsevier, 2000.

[35] K.C. Russell, Nucleation in solids: the induction and steady state effects, Adv. Colloid Interface Sci. 13 (3–4) (1980) 205–318.

[36] Thermo-Calc Software Precipitation Module (TC-PRISMA) User Guide, Version 2021b,. 2021.

[37] J. Jubica, Charact. Second. Carbides Low. -Alloy. Martensitic Model Alloy. Tool. Steels 2020.

[38] M. Lai, Y. Li, L. Lillpopp, D. Ponge, S. Will, D. Raabe, On the origin of the improvement of shape memory effect by precipitating VC in Fe–Mn–Si-based shape memory alloys, Acta Mater. 155 (2018) 222–235.

[39] K. Miao, Y. He, N. Zhu, J. Wang, X. Lu, L. Li, Coarsening of carbides during different heat treatment conditions, J. Alloy. Compd. 622 (2015) 513–523.

[40] Y. Yang, J.T. Busby, Thermodynamic modeling and kinetics simulation of precipitate phases in AISI 316 stainless steels, J. Nucl. Mater. 448 (1–3) (2014) 282–293.

[41] T. Gladman, The Physical Metallurgy of Microalloyed Steels, Maney Pub, 1997.

[42] D.B. Williams, C.B. Carter, *The Transmission Electron Microscope*, in *Transmission Electron Microscopy*, Springer, 1996, pp. 3–17.